Persistent asperities at the Kermadec subduction zone controlled by changes in forearc structure: 1976 and 2021 doublet earthquakes

Earth Planet. Sci. Lett. 624 (2023) 118465

Contents lists available at ScienceDirect

Earth and Planetary Science Letters

journal homepage: www.elsevier.com/locate/epsl

Persistent asperities at the Kermadec subduction zone controlled by changes in forearc structure: 1976 and 2021 doublet earthquakes

K. Lythgoe [a,b,*], K. Bradley [b], H. Zeng [b,c], S. Wei [b,c,*]

[a] School of Geosciences, University of Edinburgh, Scotland
[b] Earth Observatory of Singapore, Nanyang Technological University, Singapore
[c] Asian School of the Environment, Nanyang Technological University, Singapore

ARTICLE INFO

Edited by: Dr H Thybo

Keywords:
Megathrust earthquakes
Asperities
Kermadec subduction
Doublet earthquakes
Basal erosion
Seismic cycle

ABSTRACT

To what degree large earthquakes are 'characteristic' is a critical question in understanding the fundamentals of earthquake physics and the seismic cycle. Here we study the ruptures of the 2021 Mw7.4 and Mw8.1 doublet earthquake sequence in the Kermadec subduction zone and compare them with the 1976 doublet that occurred at the same location. We find that although the 2021 mainshock likely re-ruptured the same asperity as the 1976 Mw7.9 event, the detailed slip distribution is different. Other ruptures in the doublets also differ in character and location. Our observations indicate the variability between large earthquakes on the same segment of the plate boundary in each earthquake cycle. All earthquakes occur in an isolated area of the megathrust, which is bounded by changes in the lithospheric structure of the overriding plate as indicated by bathymetric and gravity data. This high-seismicity region is coincident with an isolated forearc sedimentary basin, possibly formed by basal erosion related to seismogenesis, suggesting that seismic slip has persisted here for several million years. Refined up-dip aftershock and background seismicity focal mechanisms have a steeper dip angle than the slab interface, suggesting these events are located within the subducting oceanic slab, possibly forming a rougher plate interface that facilitates basal erosion. We conclude that the stress heterogeneity within this bounded seismogenic zone is long-lived and has produced a rich spectrum of earthquake ruptures.

1. Introduction

Repeated slip on the same section of fault with earthquakes of similar size and faulting mechanism, are so-called 'characteristic earthquakes'. Such 'characteristic' fault patches rupture repeatedly with a return time based on the stressing rate, and may be created by the existence of persistent asperities – isolated high strength regions - on the fault interface (Lay and Kanamori, 1981; Sieh, 1996). The scarcity of observations of full earthquake cycles in the modern instrumental time period, means the hypothesis of a 'characteristic' large earthquake for a given fault section is generally tested using paleoseismology (e.g. Sieh, 1981; Schwartz and Coppersmith, 1984; Klinger et al., 2011). Therefore it is unclear (1) whether the same asperity is truly re-rupturing in each earthquake cycle, and (2) how variable large events on the same fault segment are.

Rare occurrences of a complete earthquake cycle within the time of modern instrumentation are at rapidly slipping faults, particularly old oceanic subduction zones. The Tonga-Kermadec subduction zone experiences the fastest plate convergence on Earth and is one of the most seismically active. Here, the Pacific plate rapidly subducts beneath the Australian plate, with convergence rates of 90 mm/year at 25°S to 50 mm/year at 35°S (Power et al., 2012). Despite having a short historical seismicity catalogue, the Kermadec subduction zone shows high levels of seismicity, with 30 shallow magnitude M7+ events since 1917, of which three events are larger than M8+ (USGS) (Fig. 1). The vast majority of seismicity, including all documented M8+ earthquakes, occur in an specific area of the plate boundary between latitudes of 28°S and 30°S, trench-ward of Raoul Island (Fig. 1). It is not clear what factor(s) concentrate large earthquakes to this region of the plate boundary or control the along-strike distribution of seismic slip at global subduction systems more generally.

The capacity of the Kermadec subduction zone to produce giant (M9+) earthquakes is unknown. Power et al. (2012) use GPS data from a site on Raoul Island – the largest volcanic island in the Kermadec arc – to

* Corresponding authors at: School of Geosciences, University of Edinburgh, Scotland and Earth Observatory of Singapore, Nanyang Technological University, Singapore.
E-mail addresses: karen.lythgoe@ed.ac.uk (K. Lythgoe), shjwei@ntu.edu.sg (S. Wei).

https://doi.org/10.1016/j.epsl.2023.118465
Received 15 May 2023; Received in revised form 23 October 2023; Accepted 24 October 2023
Available online 6 November 2023

show that the plate interface at this location is frictionally locked to depths of at least 30 km, suggesting it is capable of producing earthquakes with magnitudes larger than 8.0. Near this location, a Mw8.1 thrust earthquake occurred at a centroid depth of 34 km in March 2021 (GCMT, Ekstrom et al., 2012) (Fig. 1). This event was preceded by a nearby Mw7.4 earthquake two hours before, also with a thrust focal mechanism but with a deeper centroid depth of 43 km (GCMT). The 2021 Kermadec earthquakes occurred at similar location as a thrust faulting earthquake sequence on 14th January 1976. The 1976 sequence involved a Mw7.8 earthquake at 47 km centroid depth followed 50 min later by a Mw7.9 event at 18 km centroid depth (GCMT). At the same location, a Ms8.1 earthquake occurred on the 1st May 1917 followed by a Ms7.7 event on 16th November 1917 (Lander and Lockridge, 1989; Nishenko, 1991). The 1917 events are thought to have occurred at shallow depths, although lack of data precludes reliable locations or focal mechanisms (Nishenko, 1991). Seismic slip at the Kermadec subduction zone therefore appears to exhibit characteristic behaviour across multiple earthquake cycles.

The Kermadec margin has potential to direct tsunami energy towards northern New Zealand (Power et al., 2012). The 2021 Kermadec earthquakes generated small tsunamis in the Pacific Ocean with the National Emergency Management Agency of New Zealand issuing a

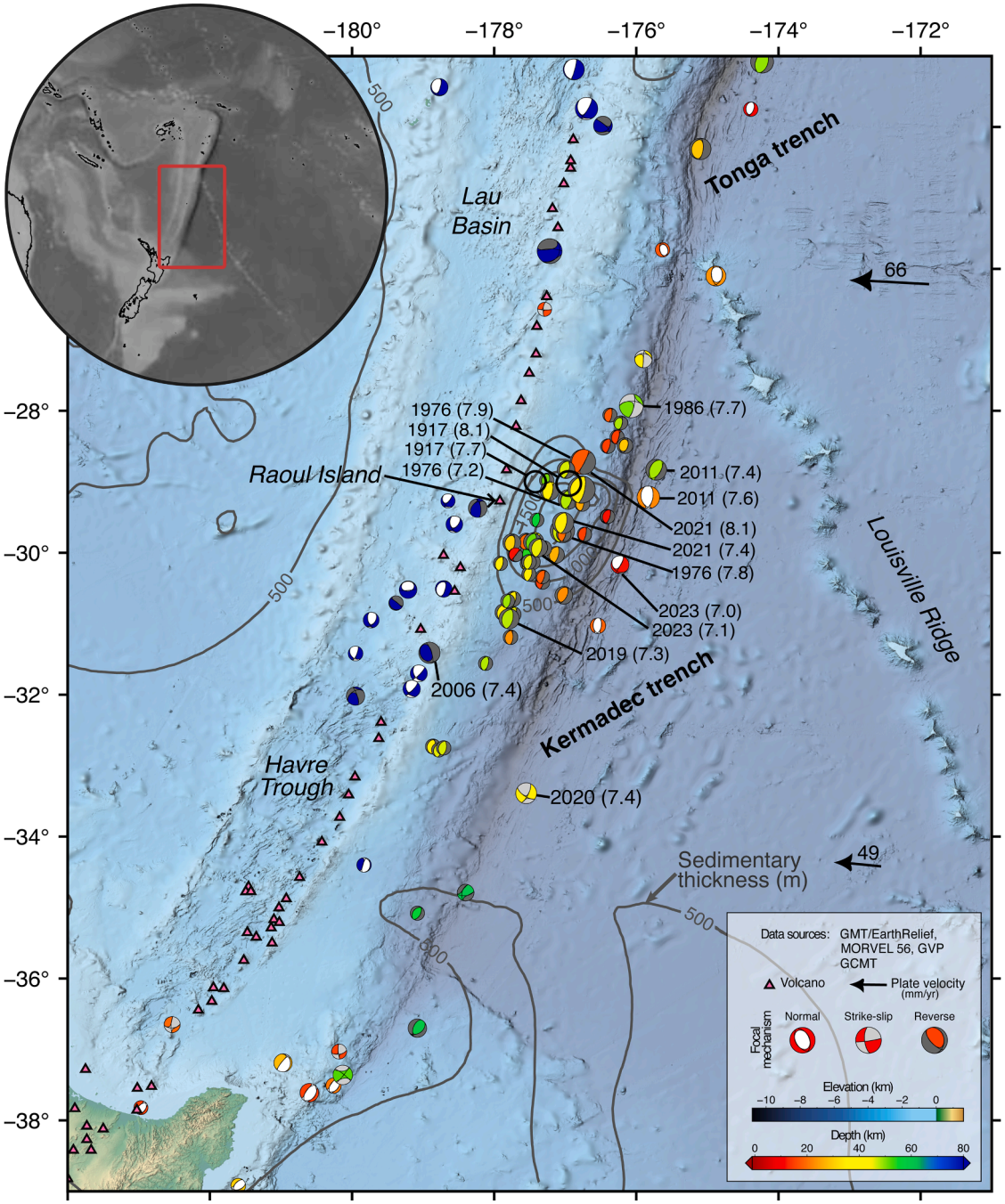

Fig. 1. Tectonic overview of the Kermadec subduction zone. Moment tensors for earthquakes with magnitude larger than 6.5 are plotted from the GCMT catalogue. Thrust focal mechanisms are plotted with dark grey dilatational quadrant, strike-slip have light grey, and normal mechanisms have a white dilatational quadrant. Locations of 1917 events are from Nishenko (1989) after Gutenberg and Richter (1954). Volcanoes are from the Global Volcanism Program. Contours are sediment thickness every 500 m from the global sediment model of Straume et al. (2019).

tsunami warning after the Mw8.1 earthquake (Romano et al., 2021). The 1976 earthquakes generated a small tsunami that was widely observed in the Pacific Ocean (Power et al., 2012), and a tsunami was reported following the 1917 events (Lander and Lockridge, 1989). Understanding the nature of seismic slip and rupture process at the Kermadec subduction zone thus has implications for seismic and tsunami hazards in the region.

The focal mechanisms and locations of the 2021 Kermadec sequence have been reported with varying degrees of completeness and large differences between different earthquake catalogues. We seek to clarify the nature of the foreshock and mainshock events, as well as produce a consistent and reliable focal mechanism catalogue to delineate active faulting structures and investigate several intriguing features in the aftershock sequence, including triggered normal faulting events and the high dip angle of thrust faulting earthquakes relative to the shallow dip angle of the plate interface.

In this study we first produce finite fault slip models for the 2021 foreshock and mainshock, and compare the location and waveforms between the 2021 and 1976 events to investigate the similarity between the large earthquakes and whether the same asperities repeatedly ruptured. We also refine the focal mechanism catalogue (including depths and locations) of medium sized aftershocks by waveform modelling to elucidate active faulting structures. We interpret our results, in combination with gravity, bathymetry and sediment thickness data, to ascertain the longevity of the seismically slipping region and the factors influencing the along-strike rupture limit of seismic slip.

2. Regional tectonics

Subduction at the Kermadec-Tonga trench has been ongoing since the middle Eocene (~45 Ma), with the plate boundary being in its current location for ~5 Myr (Wright, 1993). The plate boundary is characterised by subduction of old oceanic lithosphere (>80 Ma, Seton et al., 2020) at a sediment poor trench. The island arc system is highly active, with a high density of sub-aerial stratovolcanoes ~200 km westward of the trench (Wright, 1993). Since subduction initiation, the Pacific plate has experienced eastward trench rollback, creating a landscape of extinct volcanic ridges and back-arc basins in the over-riding plate (Schellart et al., 2006). Crustal extension in the over-riding Australian plate is active today. Back-arc rifting began in the late Miocene (~5 Ma, Ruellan et al., 2003) and has formed a series of back-arc basins, known as the Havre Trough and Lau Basin in the Kermadec and Tonga back-arcs respectively (Fig. 1).

The Kermadec and Tonga subduction zones are tectonically segmented by the Louisville Ridge – a chain of seamounts on the Pacific plate that impinges obliquely on the trench (Fig. 1). Running parallel to the trench is the Tonga Ridge, an extinct volcanic arc that forms a prominent ridge in the Tonga forearc. The Tonga Ridge may continue southward into the Northern Kermadec forearc where it is buried beneath sediment, as indicated by free air gravity anomalies (Fig. S1) and seismic velocities (Collot and Davy, 1998; Bassett et al., 2016). Bassett et al. (2016) define the Central Kermadec Discontinuity, which separates the northern and central segments of the Kermadec forearc, and represents a major change in the evolution and structure of the over-riding plate.

The largest concentration of seismicity in the Kermadec subduction system lies south of the Louisville Ridge, between latitudes of 28°S and 30°S, where the 1917, 1976 and 2021 earthquake sequences occurred (Fig. 1). Several large intraslab events have also occurred in this area. Notably a 1986 Mw7.7 thrust event occurred below the plate boundary, which is interpreted to be caused by segmentation of the incoming plate (Houston et al., 1993). An intraslab doublet occurred seaward of the plate boundary in 2011, commencing with a Mw7.6 normal faulting event, followed three months later by an adjacent but deeper Mw7.4 thrust event (Todd and Lay, 2013). Shallow outer rise normal faults are also seismically active.

3. Methods

3.1. Foreshock and mainshock slip models

We derive finite fault slip models for the Mw8.1 mainshock and its Mw7.4 foreshock by inversion of teleseismic broadband body waves. We use a rectangular fault plane that is divided into smaller sub-faults to capture the finite rupture. For the mainshock the sub-fault size is 10 km along strike and 8 km along dip, and it is 5 km by 5 km for the foreshock. The strike and dip of the fault plane are defined using the GCMT solution and the USGS epicenter locations are used, with the hypocenter depth adjusted so that it falls onto the slab2 model (Hayes et al., 2018). During the inversion, we solve for the slip amplitude and direction, rise time, and rupture velocity on each sub-fault through a simulated annealing inversion algorithm (Ji et al., 2002). Here the rise time is defined as a cosine function and the duration is inverted on each sub-fault. The rupture velocity is allowed to vary from 1.5 km/s - 3.0 km/s, with an interval of 0.1 km/s, and slip amplitude can range from 0 m to 10 m, with a step of 0.5 m. We use vertical component P and tangential component SH waves and select stations to have good distance and azimuthal coverage. We remove the instrument responses (using a 0.003-10 Hz bandpass filter), convert the waveforms to displacement and apply a 1 Hz low-pass filter (Figs. S2 and S3).

3.2. Waveform comparison between 1976 and 2021 doublets

To compare the 1976 and 2021 event waveforms, we sought seismic data from stations that were active in both years (Table S1, Fig. S4). Stations active in 1976 are principally in the HGLP (high-gain long-period) network (Ekstrom and Nettles, 1997). Unfortunately almost all HGLP stations recorded clipped waveforms for the 1976 events (Fig. S5). Waveforms at very long periods (~135 s) used in the CMT inversion are not clipped, but such long-periods are not helpful for our waveform comparison and instead we are interested in periods of around 30 s (approximately the time of the moment-rate functions). Station ZLP in Bolivia is the only station in the HGLP network to record non-clipped vertical component P-waves. Station MAT in Japan (later re-named to MAJO) had additional short and intermediate period channels which are not clipped. Two additional stations recorded non-clipped waveforms in 1976 and were operational in 2021 - these stations are GUMO (in Gaum) and ANMO (in Albuquerque, USA) in the SR (Seismic Research Observatory) network (Peterson et al, 1976). Lastly, station KHC in the Czech Republic (CZ network) - one of the oldest continuous broadband stations (Kolar, 2020) - was active in both years. We remove the instrument responses and calibrate the 1976 waveform data (Appendix A).

3.3. Focal mechanisms, depth determination and relocation of 2021 aftershocks

Focal mechanisms and locations of the 2021 Kermadec sequence vary substantially between earthquake catalogues (Fig. S6). We therefore refine the focal mechanisms, depth and location of the largest aftershocks (M>~5) through regional and teleseismic waveform modelling. We first determine focal mechanisms by inverting seismic waveforms from all available regional data, which consists of thirty seismic stations. The station distribution is limited since there are few ocean island stations, which results in an azimuthal gap between ~90°-180° (Fig. S7). We calculate focal mechanisms using the cut-and-paste technique (Zhu and Helmberger, 1996), which cuts the seismogram into five phase windows and models each window separately. Different time shifts are allowed to maximise the cross-correlation between observations and synthetics in each phase window, which reduces the sensitivity of the inversion to the accuracy of the Green's functions, thus overcoming uncertainties in the velocity model. The 1D regional velocity model used is from a nearby seismic reflection profile (Funnell et al., 2017) and continued to depth using PREM. The model space is

sampled using a Markov-Chain Monte Carlo (MCMC) scheme (Shi et al. 2018), which efficiently samples all source parameters simultaneously to converge to a global minimum. Using a MCMC approach allows us to analyse the uncertainty in our inversion using the posterior probability distribution function (PDF). For each event, we run ~2000 model updates and discard the first 10 % of models before uncertainty analysis. We use higher frequency waveforms than in GCMT to overcome the trade-off between fault dip and depth for long-period focal mechanism waveform inversion routines (Tsai et al., 2011).

After obtaining the best-fitting focal mechanism, earthquake depth is searched for independently using high-frequency teleseismic P waveforms, since these are more sensitive to depth than low frequency waveforms. We select only high-quality waveforms that contain a clear depth phase, which places tight constraints on source depth. Relatively high frequency (0.5-1.5 Hz) velocity waveforms are used for earthquakes with magnitude < 6, since these have a relatively simple source-time function (Fig. S8). For earthquakes with magnitude > 6, the waveforms are more complex, and so lower frequency (0.02-0.2 Hz) displacement waveforms are used (Fig. S9). We estimate uncertainties in depth statistically by using the range of best-fitting depths from all stations (Fig. S9).

To refine the horizontal locations, we apply a surface wave relocation method developed by Wang et al. (2018). We select a thrust (05/03/2021 14:24) and normal (05/03/2021 12:05) event as master events to relocate other thrust and normal events respectively. These events are selected as master events primarily because their USGS and GCMT locations differ by less than 15 km and the depth of the thrust event is consistent with the slab2 model. We calculate the cross-correlation functions for Rayleigh (Love) waves in radial and vertical (transverse) components recorded at the same station for the master and target events, search for the time shift that maximizes the cross-correlation functions, and only keep those time shifts with cross-correlation coefficients > 0.75. We set the theoretical range of group velocities to be 3.7-4.0 km/s and 4.0-4.3 km/s for Rayleigh and Love waves respectively, filter waveforms to 0.015-0.05 Hz, and conduct the cross-correlation in a window 100 s before and 400 s after the arrivals corresponding to the maximum and minimum group velocities. The obtained time shifts can be treated as the difference between real and predicted arrival times using the catalog earthquake locations (including a constant corresponding to the origin time error). Theoretically, any mis-location causes a sinusoidal relationship between the station azimuth and the corresponding time shift (Fig. S10). Thus, we fit these curves with a sinusoidal function and further relocate events relative to the reference events (Fig. S10). To quantify the location uncertainty, we generate synthetics for all events with focal mechanisms refined in this study, and obtain the time shifts following the same relocation procedure. For simplicity, we put all the events at the same location, and set stations at azimuths of 0-360° (6° spacing) and distances 30°, 60°, 90° from the source. One example of the obtained time shifts for a thrust event is shown in Fig. S10c. We find the maximum and average mis-locations are ~8 km and ~4 km (Fig. S10c). To be more conservative, we assume the uncertainty is 8 km.

In total we obtain moment tensor, depth and relocation solutions for 31 events with magnitude larger than 5 that occurred within two months after the mainshock (Fig. S11). We additionally re-locate the Mw7.1 aftershock that occurred two years after the mainshock in April 2023.

4. Results

4.1. Foreshock and mainshock slip models

Seismic waveforms of the mainshock (Fig. S2) and the resulting slip model (Fig. 2) are relatively simple, indicating the rupture of a single major asperity. Rupture dimensions of the peak slip patch (>3 m slip)

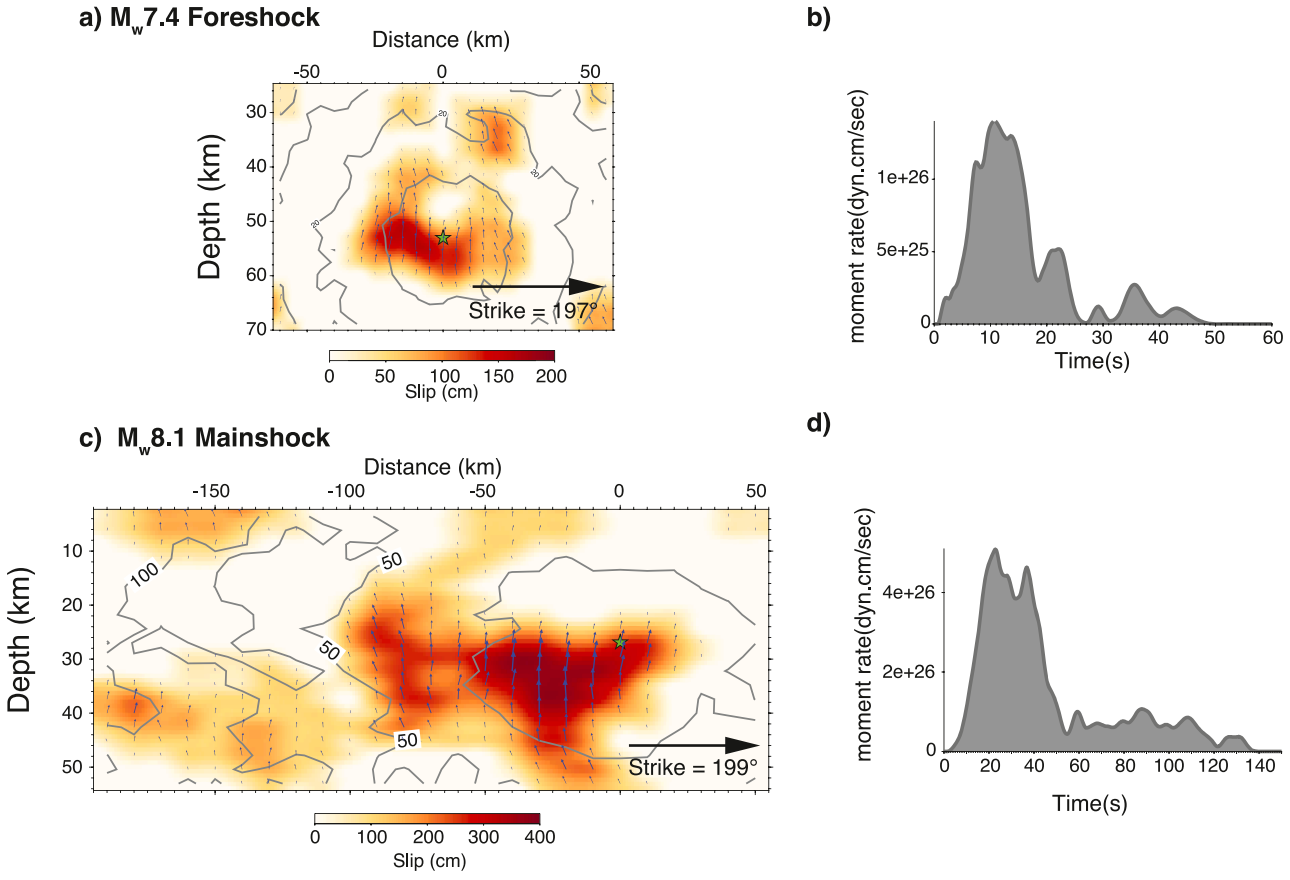

Fig. 2. Co-seismic slip and moment rate functions of the Mw7.4 foreshock (a, b) and Mw8.1 mainshock (c, d).

are approximately 100 km along strike and 60 km along dip (Fig. 2). The largest slip occurred down-dip of the hypocenter, with peak slip occurring at ~35 km depth. The lack of shallow slip explains why only small tsunami wave heights were generated (Romano et al., 2021). We find a peak co-seismic slip of 3.3 m, which is similar to the 3.15 m slip deficit accumulated on the plate boundary since the 1976 earthquakes, assuming plate motion of 70 mm/yr and 100 % coupling on the plate boundary. This indicates that much of the convergence at this asperity on the plate boundary is accommodated seismically. We note that teleseismic finite fault inversions tend to underestimate the peak slip of megathrust earthquakes, therefore 3.3 m should be considered as the lower bound of peak slip during the Mw8.1 event.

The Mw 7.4 foreshock ruptured at deeper depths, with the hypocenter at ~43 km depth (NEIC). Rupture dimensions of the peak slip patch (>~1m slip) are approximately 50 km along strike and 30 km along dip (Fig. 2). The centroid of the co-seismic rupture is ~55 km in

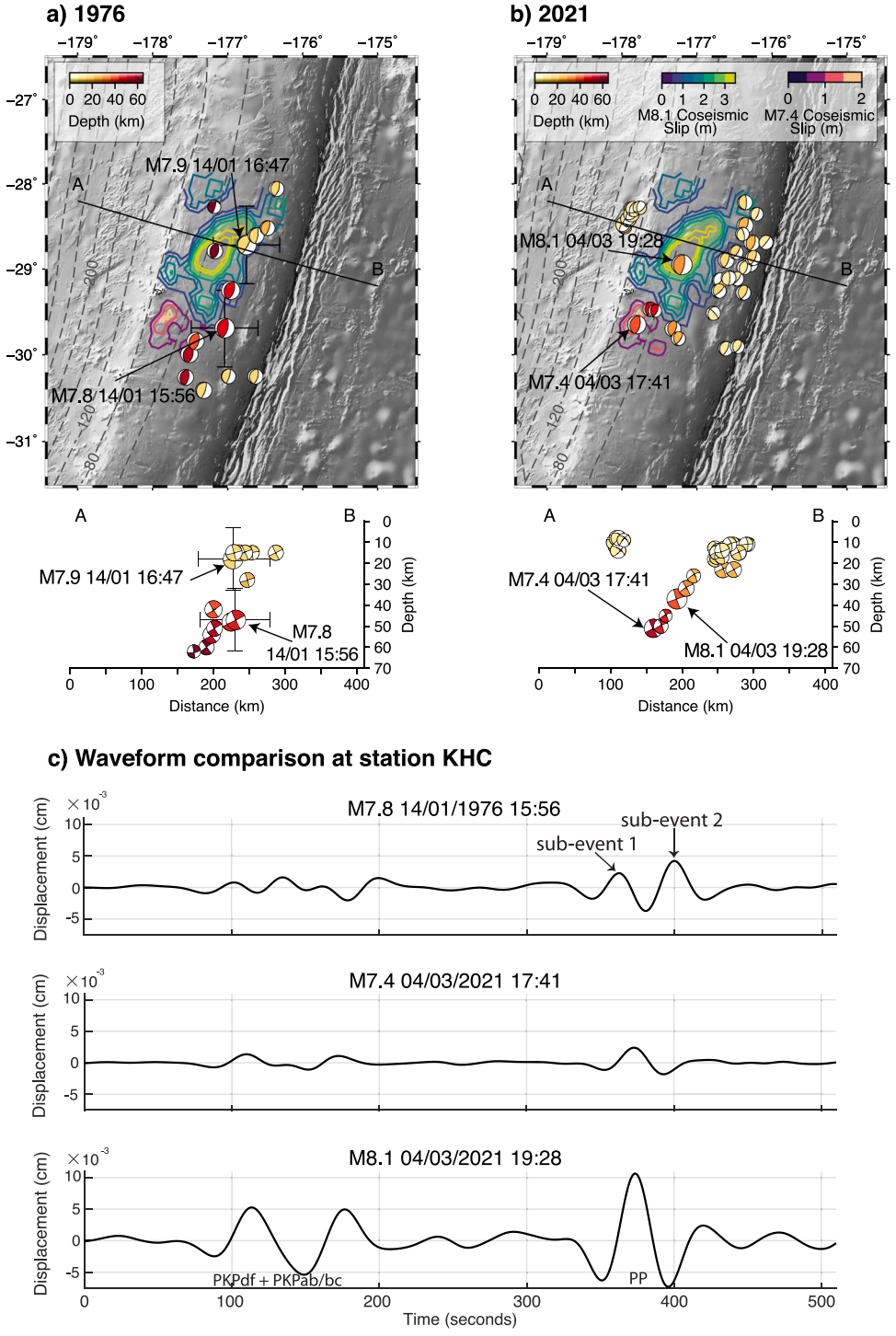

Fig. 3. Comparison of 1976 and 2021 earthquake sequences. (a) Focal mechanisms in 1976 sequence from GCMT. The horizontal location uncertainty of the Mw7.8 and Mw7.9 is assumed to be 50 km and their depth uncertainty is assigned as 15 km. (b) Focal mechanisms in the 2021 sequence from this work. The foreshock and mainshock are plotted at their centroid location determined by our slip models with the GCMT focal mechanism. (c) Vertical component waveforms recorded at station CZ.KHC in Czech Republic. Waveforms have instrument response removed and are low-pass filtered at 30 s.

depth. Failure of this deeper part of the plate interface increased stress on the up-dip area where the hypocenter of the mainshock is located and the rupture was triggered a few hours later.

4.2. Comparison between 1976 and 2021 doublets

Based on the slip distribution of the mainshock and an estimation of location uncertainties in the 1976 GCMT solutions, it is likely that the mainshock rupture area partially overlapped with the 1976 Mw7.9 event (Fig. 3). We assume conservative location errors of 50 km horizontally and 15 km in depth for the 1976 events, rather than use the reported CMT errors which do not account for systematic errors such as from incomplete Earth structure (e.g. Valentine and Trampert, 2012). Only small tsunamis were reported from the 1976 events, implying there was little shallow seismic slip and therefore any source mislocation is likely further from (not towards) the trench. This would place the 1976 Mw7.9 centroid firmly within the high slip region of the 2021 Mw8.1 event. The 2021 Mw7.4 and 1976 Mw7.8 events occurred at deeper depths and their spatial overlap is less clear, since the rupture area of the Mw7.4 event is much smaller than the mainshock and the slip model of the 1976 Mw7.8 event is not available (Fig. 3).

To further compare these events, we investigate their waveforms at the five seismic stations that were active at both times and recorded good quality waveforms at our frequency range of interest (Table S1). We first investigate the characteristics of the direct P-waves to understand the similarity in the source time functions. Waveforms for station KHC are shown in Fig. 3 and for other stations in Fig. S12. As KHC is 158° away from the earthquakes, the first P-wave arrival is dominated by the PKP triplication followed by the PP phase (Fig. 3c). We filtered the waveforms to 30 s and longer period because the 2021 mainshock moment-rate function is dominated by a single pulse of ~30 s width. Here we cannot include the 1976 Mw7.9 waveform for comparison as it was contaminated by the coda of the Mw7.8 event. The amplitude ratio (2.3) between the Mw8.1 2021 mainshock to the Mw7.8 1976 event is quite consistent with their moment ratio (2.67). The waveforms show that the 1976 Mw7.8 event is more complicated and longer lasting than either of the 2021 earthquakes (Fig. 3c). It appears that the 1976 Mw7.8 event has a more complex rupture process involving two main asperities (see also Hartzell and Heaton, 1985), whereas the waveforms and rupture model of the 2021 events indicate they can be considered as a point source (at 30 s and longer periods) and they were dominated by a single asperity rupture (Fig. 2).

Long-period waveforms of the 1976 Mw7.9 event are noisy, being contaminated by the surface waves from the earlier event. We can also investigate higher frequencies using station MAT, which was equipped with both intermediate and short period sensors, however the instrument response is not available for these channels to allow absolute amplitude comparison. From station MAT, we see that the S-waves of the 1976 Mw7.9 event are marginally larger than the Mw7.8 event, while its surface wave amplitude is slightly lower (Fig. 4). The amplitude contrast is further confirmed at 0.005–0.03 Hz (Fig. 4b), where the Mw7.9 event has a simpler waveform compared with the Mw7.8. Indeed, the Mw7.9 waveform is more similar to the Mw8.1 2021 event, with relatively high cross-correlations between the three-component waveforms, including the coda (Figs. 4, S13). The similarity between the 2021 Mw8.1 and 1979 Mw7.9 can also be seen at long-periods at station GUMO, which is the closest seismic station and so least contaminated by the earlier event's coda (Fig. S14). Given the waveform similarity and spatial overlap, it is highly possible that the 2021 Mw8.1 event re-ruptured the asperity of the 1976 Mw7.9 event.

To further understand the source properties of the 1976 events, we compare their relative strengths at higher frequencies (Fig. 4), and find that the Mw7.8 event has much more high frequency energy (by a factor of 3) than the Mw7.9 event. This amplitude contrast is consistent with that recorded at broadband station KHC (Fig. S14), and indicates a more heterogenous stress condition at the Mw7.8 source area. Waveform comparisons of the 1976 and 2021 events show that the high frequency (0.5–2.0 Hz) radiation of the 2021 Mw8.1 event is higher than the 1976

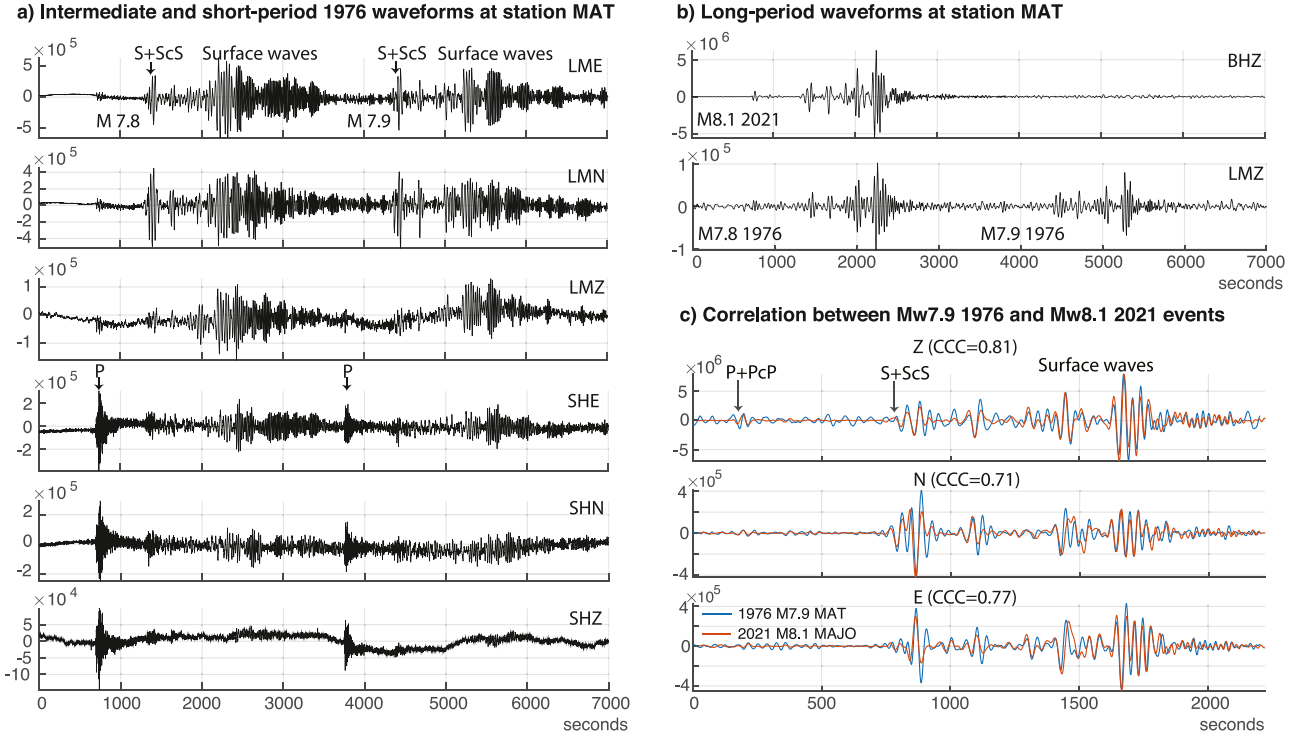

Fig. 4. Comparison of waveforms recorded at station MAT (MAJO, distance 78°, azimuth 324°). a) Intermediate period (upper three traces) and short period (lower three traces) three component waveforms for the 1976 events. b) Long period (0.005 – 0.03 Hz) vertical component waveforms or the 2021 Mw8.1 event (upper trace) and 1976 events (lower trace). c) Comparison of three-component waveforms for Mw7.9 1976 event (blue) and Mw8.1 2021 event (orange), with cross-correlation coefficients (CCC) indicated. Waveforms are filtered 0.005 – 0.03 Hz and the Mw8.1 has been scaled to the Mw7.9 event for plotting.

Mw7.9 event and at a similar level to the 1976 Mw7.8 event (Fig. S15). Given the depth dependency of high-frequency radiation from the seismogenic zone (e.g. Lay et al., 2012; Yao et al., 2013), it is most likely that although the 2021 Mw8.1 and 1976 Mw7.9 events partially overlapped, the Mw8.1 event ruptured a larger along dip dimension.

4.3. Co-location of seismic slip with an isolated, deep sedimentary basin

Sedimentary cover in the Kermadec subduction system is generally less than several hundred metres thick in the entire area (Fig. 1). However, there is one notable exception, which is an isolated sedimentary basin, over 2 km in thickness, located in the high-seismicity region between 28°S and 30°S, directly above the 1917, 1976 and 2021 earthquakes (Figs. 1; 5a, Straume et al., 2019). The co-location between this isolated sedimentary basin and the highest density of large plate interface earthquakes in Kermadec (Fig. 1) suggests a correlation between the two processes.

Long-term deformation at subduction zones causes permanent anelastic deformation in the over-riding plate. Basal erosion is one long-term anelastic process, whereby the base of over-riding plate is eroded by the subducting slab. Basal erosion thins the forearc, resulting in subsidence and creating the accommodation space for sediment deposition. Evidence for basal erosion includes long-term forearc subsidence (von Huene and Scholl, 1991) and isotope anomalies in arc magmas (Tonarini et al., 2011), although the mechanism is uncertain owing to lack of resolution in seismic images at these depths. Hilde (1983) propose that horst-and-graben structures on the subducting plate abrasively scrape the underside of the forearc, while von Huene et al. (2004) propose that hydrofracking, caused by fluids released from an over-pressurized plate interface, dislodge fragments in the upper plate, which get dragged into the subduction channel. Wang et al. (2010) argue that basal erosion only occurs in the co-seismic and immediate post-seismic period of large earthquakes. In their model, basal erosion occurs when the shallow, rate-strengthening part of the plate interface strengthens during large earthquakes and the overlying forearc wedge weakens. Wang et al. (2010) concentrate on the shallow part of subduction zones beneath the middle prism area, and it is unclear if their mechanism will also apply to basal erosion occurring further downdip. Another scenario for forearc extension is the activation of normal faults in the upper plate in response to co-seismic slip on the plate interface (e.g. Petersen et al., 2021). Interestingly we detect a normal faulting aftershock near the forearc Moho, at ~15 km depth (Fig. 6a). It is unlikely that this event lies on the plate interface and instead plausible that it occurred on a normal fault in the over-riding plate, although no such faults have yet been directly imaged. The correlation between the location of strong seismic megathrust coupling and forearc subsidence at Kermadec, adds to a global catalogue linking forearc sedimentary basins with seismogenesis (Song and Simons, 2003; Wells et al., 2003; Heuret et al., 2012).

Long-term subsidence at this isolated section of the Kermadec forearc indicates that seismogenesis has been confined to this region for many earthquake cycles, assuming that basal erosion is facilitated by seismic slip on the plate boundary. Estimation of the time scales involved can be gained by making some simple assumptions. Firstly we assume that up to 2.2 km of vertical subsidence has occurred in the forearc (based on the maximum depth of the forearc basin (Straume et al., 2019) and that lithospheric thinning due to basal erosion is the dominant process controlling subsidence. von Heune and Scholl (1991) estimated typical basal erosion rates of 0.2–0.5 mm/yr by compiling global observations of forearc subsidence. Assuming these rates, it would take 4.4-11 Myrs to produce 2.2 km of vertical subsidence. The plate boundary has been in its present position for ~ 5 Myr (although it may have occupied a similar position with respect to the subducting trench for longer, Wright, 1993), indicating that seismogenesis has been persistent at this section of the plate interface for much of its lifetime.

4.4. Rupture constrained by forearc structure

Seismic slip has thus been isolated to a specific patch of the plate interface at Kermadec for millions of years. Yet the fundamental

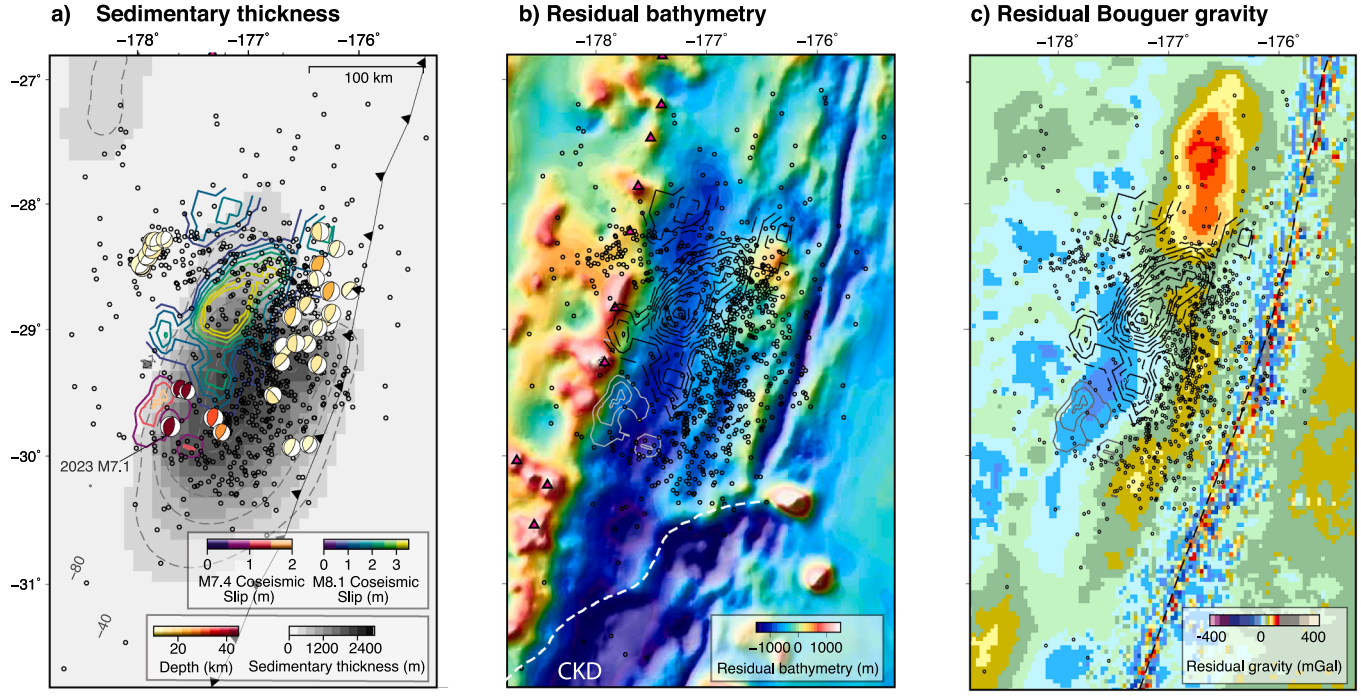

Fig. 5. (a) Co-seismic slip for the Mw7.4 and Mw8.1 2021 earthquakes, plotted with focal mechanisms determined in this study coloured by depth. The Mw7.1 2023 event is also shown. Aftershocks within the following two months from the USGS NEIC database are plotted as open circles. Sedimentary thickness from Straume et al. (2019). (b) Along-trench residual bathymetry from Bassett & Watts (2015), plotted with 2021 co-seismic slip models and two months of aftershocks. CKD = Central Kermadec Discontinuity, after Bassett et al. (2016). (c) Along-trench residual bouguer gravity field (for details of calculation see Appendix B).

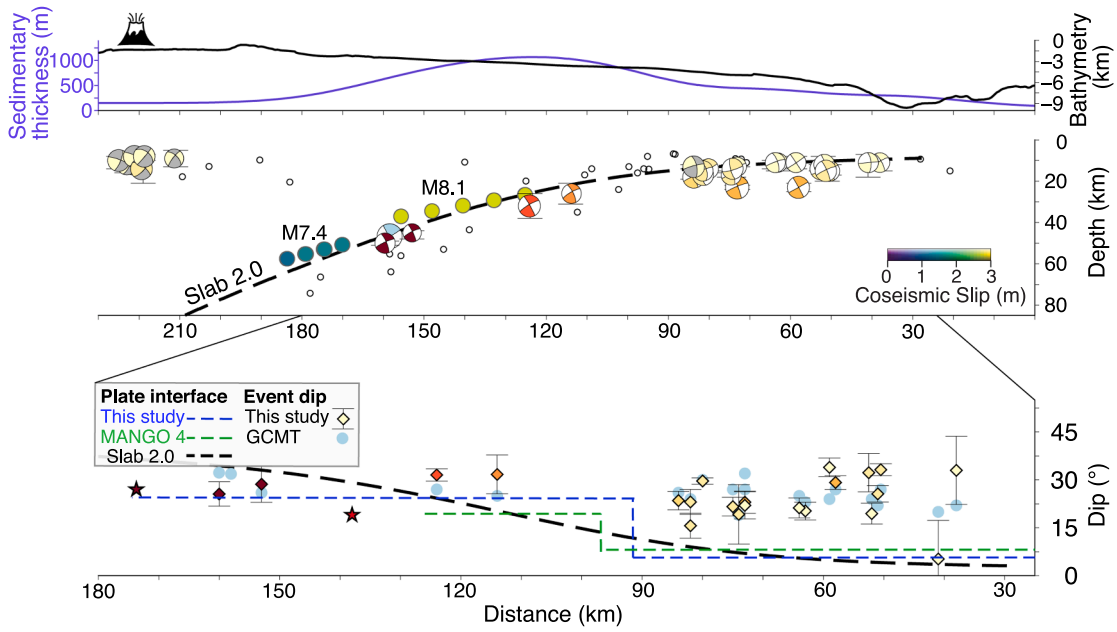

Fig. 6. Cross-section of events in the 2021 Kermadec sequence. Cross-section is same A-B line as in Fig. 3. Normal faulting aftershocks are shown with quadrants containing the pressure axis in grey. USGS aftershocks (open circles) are shown if they are not located at the default depth. Aftershock focal mechanisms are coloured by depth (see Fig. 5), while the foreshock and mainshock are plotted at their regions of highest co-seismic slip in the middle panel. The Mw7.1 2023 event is plotted in light blue. Bottom panel: fault plane dip versus distance. The foreshock and mainshock are plotted as stars coloured by depth. Values of plate interface dip are from this study (dark blue), the Mango 4 seismic reflection line (green, Bassett et al., 2016) and Slab 2.0 (black, Hayes et al., 2018).

geological reason why seismic slip occurs only at specific locations along a plate interface remains uncertain. At Kermadec, the upper plate has remained approximately stationary with respect to the deformation front for the last ~5 Myr, while the lower plate has subducted ~300 km (assuming an average convergence of 60 mm/yr). No obvious along strike variations in gravity, bathymetry and plate age are evident in the present-day surficial lower plate (Fig. S1), therefore the persistent seismic patch on the plate boundary is likely controlled by variations in the overriding plate.

Short-wavelength gravity anomalies and residual bathymetry are important to unraveling controls on slip behaviour (Song and Simons, 2003; Bassett and Watts, 2015). To investigate along strike variations, residual bathymetry is calculated by removing the average trench-normal bathymetric profile (Bassett and Watts, 2015). Likewise, we calculate the along-trench residual Bouguer gravity anomaly by subtracting the average trench-normal profile from the Bouguer corrected gravity field (Appendix B). The residual gravity field is largely sensitive to variations in forearc density.

We find that the northern edge of the 2021 Mw8.1 rupture is coincident with a positive residual Bouguer gravity anomaly in the forearc of ~100 mGal (Fig. 5). Bassett et al. (2016) interpreted positive free air residual gravity anomalies in the northern Kermadec forearc as the southward extent of the extinct volcanic Tonga Ridge. The positive gravity anomaly at the northern limit of seismic slip is spatially correlated with a fast P-wave velocity body within the lower crust of the forearc, as imaged by active source seismic refraction (Funnell et al., 2017). The gravity anomaly thus likely represents a dense body of intruded volcanic rocks within the extinct Tonga Ridge.

Dense volcanic bodies within the forearc have been suggested to control megathrust slip in other subduction zones. The most well-imaged example is at the Nankai Trough, offshore Japan. Honda and Kono (2005) detected a 'buried, large block' of dense material with a high gravity anomaly (~ 80 mGal) in the forearc near the Kii peninsula. This gravity high coincides with a forearc body of fast seismic wave speeds, which together are interpreted to be a dense, high-rigidity pluton, which appears to have acted as a barrier to the rupture propagation of Mw8+ earthquakes (Kodaira et al., 2006; Arnulf et al., 2022). The pluton causes the incoming plate to subduct at a steeper dip angle, which increases bending stresses resulting in enhanced porosity and/or fluid movement along extensional faults. Dense forearc plutons are therefore inferred to lead to an underlying weak zone of fractured ocean crust. Kodaira et al. (2006) used a rate-and-state frictional model to show that such coupling variations from an intruded pluton can act as a rupture barrier during seismic slip. Unlike at Nankai, the incoming plate is not in direct contact with the forearc crust at Kermadec, however we expect that vertical compressive stresses can be transferred through the cold, stagnant toe of the mantle wedge that behaves elastically and does not participate in mantle flow (Wada and Wang, 2009; Luo and Wang, 2021). Old and fast subduction zones, like at Kermadec, are expected to have particularly cold mantle wedge toes (Abers et al., 2017). We posit that the high gravity body at the northern limit of the 2021 co-seismic slip is from a pluton intruded into the forearc as part of the relict Eocene volcanic arc, which has persistently acted as a barrier to co-seismic rupture for the last few million years.

Controls on seismic slip to the south are more perplexing, with no gravity anomaly present. However residual bathymetry indicates a steepening at the southern limit of the slip area. This change in residual bathymetry marks the Central Kermadec Discontinuity (CKD, Bassett et al., 2016). The boundary, originally proposed by Pelletier and Dupoint (1990) to lie at a constant latitude of 32°S, was refined by Bassett et al. (2016) to lie between 32°S at the Havre Trough to 30.5°S at the plate boundary. South of the CKD, seismicity markedly reduces (Fig. 1). Further tectonic changes in the forearc include deepening of bathymetry by ~1 km, a ~15 km offset in the arc away from the trench, reduction in crustal thickness, change in strike of the remnant and active arc ridges and increase in width between the ridges (Fig. 1; Pelletier and Dupoint, 1990; Ballance et al., 1999; Bassett et al., 2016). The CKD is a structural boundary in the over-riding plate that is inherited from pre-Neogene tectonics (Bassett et al., 2016). The forearc north of the CKD is a relict Eocene arc (the Tonga Ridge), that was detached along a transform fault zone in the Oligocene (Herzer et al., 2011). Detachment was accommodated by rifting of extensional arc crust to the south, forming the Kupe Abyssal Plain. The CKD therefore represents a relict fracture zone, separating the northern Eocene arc with southern

extensional arc crust, with distinct changes in crustal thickness and lithospheric structure across the boundary (Herzer et al., 2011; Bassett et al., 2016). Structural changes in the forearc therefore appear to control the along-strike limit of seismic slip at the Kermadec plate boundary.

4.5. Fault structures inferred from aftershocks

Our relocated aftershocks approximately delineate the subducting Pacific plate interface (Fig. 6). We determine the plate interface geometry by fitting a series of best-fit lines through the aftershock locations (Fig. S16). Our two-segment plate interface model shows that at shallow depth, the plate interface dips at ~6° until approximately 15 km depth, whereby it steepens to ~25°. This model is similar to wide angle seismic reflection images acquired in the nearby area, that indicate the plate interface dips at ~8°, increasing to ~18° below ~19 km depth (Bassett et al., 2016). However, we find that events near to the trench (within ~50 km), consistently have a dip that is an average of ~18° steeper than the plate interface defined either by seismicity or seismic images (Fig. 6). Two of these events are clear intraslab events, occurring ~10 km below the inferred plate interface (Fig. 6). However, events that appear to lie on or near the plate interface also have dips steeper than the interface. Our dip angles are quite consistent with focal mechanisms reported by GCMT (Fig. 6). The discrepancies between the dip angles from earthquake focal mechanism and that from the seismic imaging are larger than the uncertainty in our focal mechanism inversions. At long-period (e.g. >100 s period), focal mechanism waveform inversion is subject to a dip-depth trade-off when the dip angle is small (Tsai et al., 2011). Here we use shorter period (e.g. 10-100 s) waveforms to suppress such trade-off. We further verify the focal mechanism of a representative thrust event using high frequency teleseismic waveforms, in which the dip obtained using regional waveforms is 27.5°+/-1.1° and 26.3°+/-3.5° using teleseismic waveforms (Fig. S17).

Using relatively high frequency waveforms, Zhan et al. (2012) also found that fault plane dips are greater than the plate interface dip in the source region of the 2011 Mw9.1 Tohoku-Oki earthquake. They proposed that the discrepancy indicated the plate boundary may be undulating and/or that the aftershocks occur on sub-faults near to the plate interface. Seismic reflection studies in the Kermadec area (Bassett et al., 2016; Funnel et al., 2017) report no evidence for an undulating plate boundary at depth, although this is likely below imaging resolution. Reflection images do show graben structures in the crust of the subducting Pacific plate, and seismic refraction studies report low crustal seismic velocities, indicative of a fractured oceanic lithosphere. Re-activation of such faults in the subducted oceanic crust following rupture of the plate interface could occur, although their dip is likely greater than we observe. An alternative explanation, suggested by Singh et al. (2012) based on interpretation of reflection images offshore Sumatra, is that the megathrust at these depths is now in the mantle, and the steeply dipping aftershocks represent faults in oceanic crust that is being underplated. However, with no further evidence, we deem this unlikely. Instead, the shallow aftershocks are most consistent with being driven by flexural slip – this process produces thrust earthquakes just below the plate interface with fault planes sub-parallel to the top of the slab (Romeo and Álvarez-Gómez, 2018).

Thirteen Mw>5 aftershocks occurred with normal faulting mechanisms in the two months after the mainshock (Fig. 5). One of these events (Mw6.15 on 29th April 2021) occurred close to the megathrust interface at ~13 km depth. The others form a distinct cluster of shallow normal faulting aftershocks, which occurred two days after the mainshock in the over-riding Australian plate, over 200 km from the trench (Fig. 5). The extensional events occur in the back-arc basin, known as the Havre Trough (Fig. 1). Active extension is occurring in the Havre Trough, with normal faults in over-riding plate imaged on seismic reflection data to the north (Funnel et al., 2014), possibly indicating the presence of a graben structure due to back-arc opening. Existing normal faults in the Havre Trough were likely activated by static stress changes from the mainshock sequence.

5. Discussion and conclusion

Doublet magnitude 7-8 earthquakes have ruptured the same area of the Kermadec megathrust every 52+/-7 years, since the first recorded earthquake here in 1917. We found that all of the plate convergence since the last earthquake sequence in 1976, was accommodated by co-seismic slip in the 2021 earthquake sequence. This indicates that all or most convergence is accommodated by seismic slip on the megathrust at these asperities, implying strong mechanical coupling between the over-riding Australian plate and under thrusting Pacific plate here.

Although a similar portion of the plate interface re-ruptured in 1976 and 2021, comparison of locations and waveforms between these earthquake sequences indicate different slip distributions (see Fig. 7 for a schematic). The 2021 Mw8.1 earthquake ruptured one major asperity, which is similar in location and waveform character to the 1976 Mw7.9 event, but note that the Mw8.1 likely ruptured a larger along dip and strike dimension. In contrast, the 1976 Mw7.8 event ruptured at least two major asperities. Given its spatial proximity to the 2021 Mw7.4 event, it is possible that one of these asperities also ruptured in the 2021 sequence. A subsequent Mw7.1 thrust event occurred on the plate boundary in 2023, close to the 2021 Mw7.4 foreshock (Fig. 5a), suggesting the presence of a heterogeneous fault patch that had residual strain energy. It is possible that this patch may have additionally slipped in the 1976 Mw7.8 event. Re-rupture of similar asperities has been studied in other subduction zones. Investigating the asperity distribution of large (M7.5+) earthquakes along the New Britain trench at Papua New Guinea, Park and Mori (2007) concluded it was unlikely that the same asperities ruptured in each earthquake, while Tanioka et al. (1996) also conclude that different asperities ruptured in 1967 (M8.1) and 1994 (M7.7) megathrust earthquakes offshore Japan. On the other hand, Nocquet et al. (2017) and Ye et al. (2016) find probable re-rupture of the same asperity in 1942 (M7.8) and 2016 (M7.8) earthquakes at the Ecuador subduction zone. Here we conclude that asperities can be long-lived persistent features, but they will fail in different areas or patterns depending on the slip distribution at each earthquake cycle, which is consistent with numerical modelling (Hirose and Hirahara 2002). Therefore although large earthquakes may appear very similar, such as in this region of the Kermadec megathrust, their detailed ruptures differ due to stress heterogeneities imparted by the rupture of earthquakes in the interseismic cycle.

Large earthquakes repeatedly occur at the same section of the plate interface at Kermadec which is co-located with a prominent sedimentary basin in the forearc, implying that forearc subsidence is generated by seismic slip and that seismic rupture of this section of the plate interface is persistent. The co-seismic slip region is bound to the north by a change in forearc structure as indicated by a large gravity anomaly and to the south by the Central Kermadec Discontinuity marking a pronounced change in lithospheric structure. The confined along-strike seismic slip may explain why the maximum recorded earthquake magnitude in this region is Mw8.1. Other island-arc subduction zones also have maximum recorded megathrust earthquake magnitudes of about Mw8.1 (including Vanuatu, Solomon Islands, Sulawesi, and the Philippines), and may be similarly bound by structural changes in the forearc.

An additional complexity at Kermadec is that large earthquakes consistently occur in closely related doublets, separated by hours or days. Large (M7+) earthquake doublets are also observed at subduction zones in the Solomon Islands and Papua New Guinea (Lay and Kanamori, 1980; Park and Mori 2007). The presence of distributed large asperities that have similar size is proposed to explain this doublet behaviour, such that failure of one asperity increases stress in nearby areas, triggering slip on an adjacent asperity (Lay and Kanamori, 1981; Ruff and Kanamori, 1983). A pressing question is whether large, distributed asperities could rupture at the same time as a larger event, as

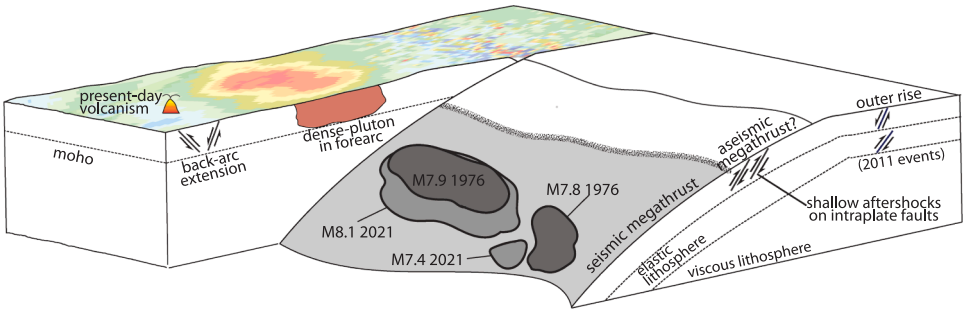

Fig. 7. Schematic illustrating seismic and tectonic structures in the Kermadec subduction zone between 27°S to 30°S and relationship between the 1976 and 2021 doublets.

shown in numerical simulations (Kaneko et al., 2010) and earthquake cycle observations (Philibosian and Meltzner, 2020). A notable observational case is in Sumatra, where sequences of M7.5+ earthquakes occurred along sections of the megathrust that eventually ruptured in the single Mw9.1 2004 event.

Our refined earthquake catalogue for the 2021 sequence shows that shallow thrust faulting aftershocks, with well-constrained fault dips and horizontal locations, likely occur on faults penetrating the oceanic crust (Fig. 7). These events may help to form a rougher plate interface that facilitates basal erosion. On the other hand, these events may suggest that the up-dip portion of the Kermadec megathrust largely slipped aseismically in this earthquake sequence. Aseismic shallow megathrusts are often attributed to the presence of velocity-strengthening clay minerals in the fault zone or high pore-fluid pressure from subducting sediments (Marone and Scholz, 1988; Bedford et al., 2021). The Kermadec trench is sediment poor, with no accretionary prism, yet thin sedimentary layers on the subducting plate may still be present (Funnell et al., 2017). However as the Mw9.1 2011 Tohoku and other large earthquakes have shown, a shallow aseismic region may occasionally slip seismically in great earthquakes due strong dynamic weakening mechanisms (Hubbard et al., 2015). Historical observations along the Kermadec trench span a very limited time interval, so there is large uncertainty for seismic and tsunami hazards of the region. If the Kermadec megathrust ruptured to the trench, the rupture dimension would be ~180 km in width. Assuming all asperities ruptured at the same time, yet co-seismic slip remained bound by structural barriers at the plate interface, the maximum along strike dimension is ~240 km. Scaling this slip area to the Mw9.1 Tohoku earthquake, corresponds to a possible ~Mw8.9 earthquake at Kermadec, which would have significant implications for tsunami hazards in the region.

Data availability

We use freely available seismic data from following networks: IU (doi: 10.7914/SN/IU), II (doi: 10.7914/SN/II), AU (doi: 10.26186/144675), S1 (doi: 10.7914/SN/S1), ND (doi: 10.7914/SN/ND), AK (doi: 10.7914/SN/AK), G (doi: 10.18715/GEOSCOPE.G), GE (doi: 10.14470/TR560404), CI (doi: 10.7914/SN/CI), AE (doi: 10.7914/SN/AE), AT (doi: 10.7914/SN/AT), AV (doi: 10.7914/SN/AV), AZ (doi: 10.7914/SN/AV), BK (doi: 10.7932/BDSN), C1 (doi: 10.7914/SN/C1), CC (doi: 10.7914/SN/CC), CN (doi: 10.7914/SN/CN), CU (doi: 10.7914/SN/CU, GS (doi: 10.7914/SN/GS), GT (doi: 10.7914/SN/GT), IC (doi: 10.7914/SN/IC), IW (doi: 10.7914/SN/IW), MX (doi: 10.21766/SSNMX/SN/MX), OO (doi: 10.7914/SN/OO), PY (doi: 10.7914/SN/PY), RM (doi: 10.7914/SN/RM), TW (doi: 10.7914/SN/TW), TX (doi: 10.7914/SN/TX), US (doi: 10.7914/SN/US), UU (doi: 10.7914/SN/UU), UW (doi: 10.7914/SN/UW),), CZ (doi: 10.7914/SN/CZ), HGLP (10.7914/SN/HG), SR (10.7914/SN/SR), C, YW, IM, JP, KG, KS, PS, SC, MY, HK and NZ. The earthquake catalogue and slip models derived here are available at https://doi.org/10.7488/ds/7534.

CRediT authorship contribution statement

K. Lythgoe: Conceptualization, Formal analysis, Investigation, Methodology, Project administration, Visualization, Writing – original draft. **K. Bradley:** Conceptualization, Investigation, Methodology, Writing – review & editing. **H. Zeng:** Formal analysis, Investigation, Methodology, Writing – review & editing. **S. Wei:** Conceptualization, Formal analysis, Investigation, Methodology, Writing – review & editing.

Declaration of Competing Interest

The authors declare that they have no known competing financial interests or personal relationships that could have appeared to influence the work reported in this paper.

Data availability

Data we use is all open access and we give citation to all seismic networks used in the acknowledgements. We will make products from the work available in an open repository.

Acknowledgements

We thank the Czech Regional Seismic Network for the continuous long-lived operation of station KHC (doi: 10.7914/SN/CZ) and the Albuquerque Seismological Laboratory/USGS for the operation of the SR (10.7914/SN/SR) and HGLP networks (10.7914/SN/HG). This project is supported by Singapore MOE projects MOE-MOET32021-0002 and MOE2019-T2-1-182, and the Earth Observatory of Singapore via its funding from the National Research Foundation Singapore and the Singapore Ministry of Education under the Research Centres of Excellence initiative. Additional support is from NERC award NE/W008289/1.

Supplementary materials

Supplementary material associated with this article can be found, in the online version, at doi:10.1016/j.epsl.2023.118465.

Appendix A. - Calibration of 1976 waveform data

Five stations recorded waveforms of sufficiently high-quality at our frequency range of interest (Table S1). These stations are KHC in the CZ network (in the Czech Republic), GUMO and ANMO (in Guam and the USA respectively) part of the SR (Seismic Research Observatory)

network (Peterson et al., 1976), ZLP and MAT (now renamed to MAJO, in Bolivia and Japan respectively), part of the HGLP (high-gain long-period) network (Ekstrom and Nettles, 1997). Stations in the HGLP and SR networks were equipped with long-period sensors, while station MAT had additional short and intermediate period sensors. We removed the instrument responses using pole-zero (PZ) files downloaded from the IRIS Data Management Centre. Instrument responses for long-period instruments in the HGLP and SR networks are unique to each station, and the seismometer period drifted over time (Ekstrom and Nettles, 1997). Ekstrom and Nettles (1997) estimated the instrument responses for each seismograph, however we found a large phase shift (~20 seconds) occurred when deconvolving the instrument response for stations in these networks. Waveforms were therefore shifted by aligning the first arriving energy with the predicted arrival time from a 1D Earth model. For station KHC, we found that the gain is not correct for the 1976 data, since the 1976 Mw7.8 event has an amplitude that is ~ 3 times larger than the 2021 Mw8.1 mainshock. To calibrate the amplitude for the 1976 waveforms, we looked into later records of teleseismic events that were also recorded by nearby broadband stations. A Mb6.3 earthquake in Panama in July 1976 was recorded by KHC and three nearby stations in Germany (GRA network). P-wave waveforms and amplitudes are expected to be similar between KHC and GRA stations since they are separated by only ~170 km. We removed the instrument response and found that, while their waveforms are highly similar, the KHC amplitude is 5.8 times larger than the GRA stations (Fig. S18). Since the amplitudes and waveforms between the GRA stations are highly consistent, we consider their gains are correct, and therefore an amplitude correction factor of 5.8 is needed for station KHC.

Appendix B. - Residual gravity field calculation

We use the WGM2012 global Bouguer gravity anomaly grid (Balmino et al., 2012) as the basis for our residual gravity calculation. In WGM2012, the Bouger anomaly is calculated by removing the contribution of the water column and the crust of the Earth at a global scale using spherical harmonics. This procedure removes the gravitational effect of topography, such that any remaining signal must be attributed to density variations in the subsurface departing from the reference density (Balmino et al., 2012).

Residual anomalies are calculated by subtracting along-track and across-track averages, defined by a multi-segment track drawn along the subduction trench. The input gravity grid is subsampled with bicubic spline interpolation, and the resulting XYZ grid points are projected to their closest location along the track. Each point is assigned da-dt coordinates based on the along-track distance of the projected point (da) and the signed distance to the projected point (dt). For each point in da-dt space, we calculate the mean Z value of all points that fall within along-track and across-track sliding windows. A new grid is constructed from the resulting XYZ' points, which is then up-sampled with cubic interpolation to create an average grid at the same resolution as the input grid. The residual grid is the difference between the input grid and the average grid (Fig. S19). The subsampling/upsampling process allows efficient processing of large profiles, but the procedure can be done at native resolution. The size of the along-track and across-track windows dictate how closely the average grid matches the input grid. When the along-track window is as wide as the track is long, and the across-track window is small, this method is closely equivalent to the approach of Bassett and Watts (2015), although it does not suffer from mis-ordering of points arising from drawing trench-perpendicular profiles along a wavy trench. In this study, we adopt an along-strike averaging window that is 600 km wide. The trench geometry was delineated based on the deepest part of the trench using bathymetry.

References

Abers, G.A., Van Keken, P.E., Hacker, B.R., 2017. The cold and relatively dry nature of mantle forearcs in subduction zones. Nat. Geosci. 10 (5), 333–337.

Arnulf, A.F., Bassett, D., Harding, A.J., Kodaira, S., Nakanishi, A., Moore, G., 2022. Upper-plate controls on subduction zone geometry, hydration and earthquake behaviour. Nat. Geosci. 15 (2), 143–148.

Balmino, G., Vales, N., Bonvalot, S., Briais, A., 2012. Spherical harmonic modelling to ultra-high degree of Bouguer and isostatic anomalies. J. Geod. 86 (7), 499–520.

Ballance, P.F., Ablaev, A.G., Pushchin, I.K., Pletnev, S.P., Birylina, M.G., Itaya, T., Gibson, G.W., 1999. Morphology and history of the Kermadec trench–arc–backarc basin–remnant arc system at 30 to 32° S: geophysical profile, microfossil and K–Ar data. Mar. Geol. 159 (1-4), 35–62.

Bassett, D., Watts, A.B., 2015. Gravity anomalies, crustal structure, and seismicity at subduction zones: 2. Interrelationships between fore-arc structure and seismogenic behavior. Geochem. Geophys. Geosyst. 16 (5), 1541–1576.

Bassett, D., Kopp, H., Sutherland, R., Henrys, S., Watts, A.B., Timm, C., Scherwath, M., Grevemeyer, I., de Ronde, C.E.J., 2016. Crustal structure of the Kermadec arc from MANGO seismic refraction profiles. J. Geophys. Res. Solid Earth.

Bedford, J.D., Faulkner, D.R., Allen, M.J., Hirose, T., 2021. The stabilizing effect of high pore-fluid pressure along subduction megathrust faults: Evidence from friction experiments on accretionary sediments from the Nankai Trough. Earth Planet. Sci. Lett. 574, 117161.

Collot, J.Y., Davy, B., 1998. Forearc structures and tectonic regimes at the oblique subduction zone between the Hikurangi Plateau and the southern Kermadec margin. J. Geophys. Res. Solid Earth 103 (B1), 623–650.

Ekström, G., Nettles, M., 1997. Calibration of the HGLP seismograph network and centroid-moment tensor analysis of significant earthquakes of 1976. Phys. Earth Planet. Inter. 101 (3-4), 219–243.

Ekström, G., Nettles, M., Dziewonski, A.M., 2012. The global CMT project 2004-2010: centroid-moment tensors for 13,017 earthquakes. Phys. Earth Planet. Inter. 200-201, 1–9.

Funnell, M.J., Peirce, C., Stratford, W.R., Paulatto, M., Watts, A.B., Grevemeyer, I., 2014. Structure and deformation of the Kermadec forearc in response to subduction of the Pacific oceanic plate. Geophys. J. Int. 199 (2), 1286–1302.

Funnell, M.J., Peirce, C., Robinson, A.H., 2017. Structural variability of the Tonga-Kermadec forearc characterized using robustly constrained geophysical data. Geophys. J. Int. 210 (3), 1681–1702. September.

Gutenberg, B., Richter, C.F., 1954. Seismicity of the Earth, 2nd ed. Princeton Univ. Press, New Jersey, pp. 161–234.

Hartzell, S.H., Heaton, T.H., 1985. Teleseismic time functions for large, shallow subduction zone earthquakes. Bull. Seismol. Soc. Am. 75 (4), 965–1004.

Hayes, G., Moore, G., Portner, D., Hearne, M., Flamme, H., Furtney, M., Smoczyk, G., 2018. Slab2, a comprehensive subduction zone geometry model. Science 362.

Herzer, R.H., Barker, D.H.N., Roest, W.R., Mortimer, N., 2011. Oligocene-Miocene spreading history of the northern South Fiji Basin and implications for the evolution of the New Zealand plate boundary. Geochem. Geophys. Geosyst. 12 (2).

Heuret, A., Conrad, C.P., Funiciello, F., Lallemand, S., Sandri, L., 2012. Relation between subduction megathrust earthquakes, trench sediment thickness and upper plate strain. Geophys. Res. Lett. 39 (5).

Hilde, T.W., 1983. Sediment subduction versus accretion around the Pacific. Tectonophysics 99 (2-4), 381–397.

Hirose, H., Hirahara, K., 2002. A model for complex slip behavior on a large asperity at subduction zones. Geophys. Res. Lett. 29 (22), 25-1.

Honda, R., Kono, Y., 2005. Buried large block revealed by gravity anomalies in the Tonankai and Nankai earthquakes regions, southwestern Japan. Earth Planets Space 57, e1–e4.

Houston, H., Anderson, H., Beck, S.L., Zhang, J., Schwartz, S., 1993. The 1986 Kermadec earthquake and its relation to plate segmentation. Shallow Subduction Zones: Seismicity, Mechanics and Seismic Potential Part 1. Birkhäuser, Basel, pp. 331–364.

Hubbard, J., Barbot, S., Hill, E.M., Tapponnier, P., 2015. Coseismic slip on shallow décollement megathrusts: Implications for seismic and tsunami hazard. Earth Sci. Rev. 141, 45–55.

Ji, C., Wald, D.J., Helmberger, D.V., 2002. Source description of the 1999 Hector Mine, California, earthquake, part I: Wavelet domain inversion theory and resolution analysis. Bull. Seismol. Soc. Am. 92 (4), 1192–1207.

Kaneko, Y., Avouac, J.P., Lapusta, N., 2010. Towards inferring earthquake patterns from geodetic observations of interseismic coupling. Nat. Geosci. 3 (5), 363–369.

Klinger, Y., Etchebes, M., Tapponnier, P., Narteau, C., 2011. Characteristic slip for five great earthquakes along the Fuyun fault in China. Nat. Geosci. 4 (6), 389–392.

Kodaira, S., Hori, T., Ito, A., Miura, S., Fujie, G., Park, J.O., Kaneda, Y., 2006. A cause of rupture segmentation and synchronization in the Nankai trough revealed by seismic imaging and numerical simulation. J. Geophys. Res. Solid Earth 111 (B9).

Kolář, P., 2020. The KHC seismic station: the birthplace of broadband seismology. Seismol. Res. Lett. 91 (2A), 1057–1063, 2020.

Lander, J.F., Lockridge, P.A., 1989. United States Tsunamis (Including United States Possessions) 1690-1988. National Oceanic and Atmospheric Administration, National Geophysical Data Centre, Boulder, Colorado, USA. Publication 41-2.

Lay, T., Kanamori, H., 1980. Earthquake doublets in the Solomon Islands. Phys. Earth Planet. Int. 283–304.

Lay, T., Kanamori, H., 1981. An asperity model of large earthquake sequences. Earthq. Predict. Int. Rev. 4, 579–592.

Lay, T., Kanamori, H., Ammon, C.J., Koper, K.D., Hutko, A.R., Ye, L., Rushing, T.M., 2012. Depth-varying rupture properties of subduction zone megathrust faults. J. Geophys. Res. Solid Earth 117 (B4).

Luo, H., Wang, K., 2021. Postseismic geodetic signature of cold forearc mantle in subduction zones. Nat. Geosci. 14 (2), 104–109.
Marone, C., Scholz, C.H., 1988. The depth of seismic faulting and the upper transition from stable to unstable slip regimes. Geophys. Res. Lett. 15 (6), 621–624.
Nishenko, S.P., 1991. Circum-pacific seismic potential: 1989–1999. Aspects of Pacific seismicity. Birkhäuser, Basel, pp. 169–259.
Nocquet, J.M., Jarrin, P., Vallée, M., Mothes, P.A., Grandin, R., Rolandone, F., Delouis, B., Yepes, H., Font, Y., Fuentes, D., Régnier, M., 2017. Supercycle at the Ecuadorian subduction zone revealed after the 2016 Pedernales earthquake. Nat. Geosci. 10 (2), 145–149.
Park, S.C., Mori, J., 2007. Are asperity patterns persistent? Implication from large earthquakes in Papua New Guinea. J. Geophys. Res.: Solid Earth 112, B03303. https://doi.org/10.1029/2006JB004481.
Pelletier, B., Dupont, J., 1990. Érosion, accrétion, extension arrière-arc et longueur du plan de subduction le long de la marge active des Kermadec, Pacifique Sud-Ouest. R. Acad. Sel. Paris 310, 1657–1664.
Petersen, F., Lange, D., Ma, B., Grevemeyer, I., Geersen, J., Klaeschen, D., Kopp, H., 2021. Relationship between subduction erosion and the up-dip limit of the 2014 Mw 8.1 Iquique earthquake. Geophys. Res. Lett. 48 (9).
Peterson, J., Butler, H.M., Holcomb, L.G., Hutt, C.R., 1976. The seismic research observatory. Bull. Seismol. Soc. Am. 66 (6), 2049–2068.
Philibosian, B., Meltzner, A.J., 2020. Segmentation and supercycles: a catalog of earthquake rupture patterns from the Sumatran Sunda Megathrust and other well-studied faults worldwide. Quat. Sci. Rev. 241, 106390.
Power, W., Wallace, L., Wang, X., Reyners, M., 2012. Tsunami hazard posed to New Zealand by the Kermadec and southern New Hebrides subduction margins: an assessment based on plate boundary kinematics, interseismic coupling, and historical seismicity. Pure Appl. Geophys. 169 (1), 1–36.
Romano, F., Gusman, A.R., Power, W., Piatanesi, A., Volpe, M., Scala, A., Lorito, S., 2021. Tsunami source of the 2021 M_W 8.1 Raoul island earthquake from DART and tide-gauge data inversion. Geophys. Res. Lett. 48 (17).
Romeo, I., Álvarez-Gómez, J.A., 2018. Lithospheric folding by flexural slip in subduction zones as source for reverse fault intraslab earthquakes. Sci. Rep. 8 (1), 1–9.
Ruellan, E., Delteil, J., Wright, I., Matsumoto, T., 2003. From rifting to active spreading in the Lau Basin–Havre Trough backarc system (SW Pacific): Locking/unlocking induced by seamount chain subduction. Geochem. Geophys. Geosyst. 4 (5).
Ruff, L., Kanamori, H., 1983. The rupture process and asperity distribution of three great earthquakes from long-period diffracted P-waves. Phys. Earth Planet. Inter. 31 (3), 202–230.
Schellart, W.P., Lister, G.S., Toy, V.G., 2006. A late cretaceous and cenozoic reconstruction of the southwest pacific region: tectonics controlled by subduction and slab rollback processes. Earth Sci. Rev. 76 (3-4), 191–233.
Schwartz, D.P., Coppersmith, K.J., 1984. Fault behavior and characteristic earthquakes: Examples from the Wasatch and San Andreas fault zones. J. Geophys. Res. Solid Earth 89 (B7), 5681–5698.
Seton, M., Müller, R.D., Zahirovic, S., Williams, S., Wright, N., Cannon, J., Whittaker, J., Matthews, K., McGirr, R., 2020. A global dataset of present-day oceanic crustal age and seafloor spreading parameters. Geochem. Geophys. Geosyst.
Shi, Q., Wei, S., Chen, M., 2018. An MCMC multiple point sources inversion scheme and its application to the 2016 Kumamoto M w 6.2 earthquake. Geophys. J. Int. 215 (2), 737–752.
Sieh, K.E., 1981. A review of geological evidence for recurrence times of large earthquakes. Earthq. Predict. Int. Rev. 4, 181–207.
Sieh, K., 1996. The repetition of large-earthquake ruptures. Proc. Natl. Acad. Sci. 93 (9), 3764–3771.
Singh, S.C., Chauhan, A.P., Calvert, A.J., Hananto, N.D., Ghosal, D., Rai, A., Carton, H., 2012. Seismic evidence of bending and unbending of subducting oceanic crust and the presence of mantle megathrust in the 2004 Great Sumatra earthquake rupture zone. Earth Planet. Sci. Letters 321, 166–176.
Song, T.R.A., Simons, M., 2003. Large trench-parallel gravity variations predict seismogenic behavior in subduction zones. Science 301 (5633), 630–633.
Straume, E.O., Gaina, C., Medvedev, S., Hochmuth, K., Gohl, K., Whittaker, J.M., et al., 2019. GlobSed: updated total sediment thickness in the world's oceans. Geochem. Geophys. Geosyst. 20.
Tanioka, Y., Ruff, L., Satake, K., 1996. The Sanriku-oki, Japan, earthquake of December 28, 1994 (Mw 7.7): rupture of a different asperity from a previous earthquake. Geophys. Res. Lett. 23 (12), 1465–1468.
Todd, E.K., Lay, T., 2013. The 2011 Northern Kermadec earthquake doublet and subduction zone faulting interactions. J. Geophys. Res. Solid Earth 118 (1), 249–261.
Tonarini, S., Leeman, W.P., Leat, P.T., 2011. Subduction erosion of forearc mantle wedge implicated in the genesis of the South Sandwich Island (SSI) arc: evidence from boron isotope systematics. Earth Planet. Sci. Lett. 301 (1-2), 275–284.
Tsai, V.C., Hayes, G.P., Duputel, Z., 2011. Constraints on the long-period moment-dip trade-off for the Tohoku earthquake. Geophys. Res. Lett. 38 (7).
Valentine, A.P., Trampert, J., 2012. Assessing the uncertainties on seismic source parameters: Towards realistic error estimates for centroid-moment-tensor determinations. Phys. Earth Planet. Inter. 210, 36–49.
von Huene, R., Scholl, D.W., 1991. Observations at convergent margins concerning sediment subduction, subduction erosion, and the growth of continental crust. Rev. Geophys. 29 (3), 279–316.
von Huene, R., Ranero, C.R., Vannucchi, P., 2004. Generic model of subduction erosion. Geology 32 (10), 913–916.
Wada, I., Wang, K., 2009. Common depth of slab-mantle decoupling: Reconciling diversity and uniformity of subduction zones. Geochem. Geophys. Geosyst. 10 (10).
Wang, K., Hu, Y., Von Huene, R., Kukowski, N., 2010. Interplate earthquakes as a driver of shallow subduction erosion. Geology 38 (5), 431–434.
Wang, X., Bradley, K.E., Wei, S., Wu, W., 2018. Active backstop faults in the Mentawai region of Sumatra, Indonesia, revealed by teleseismic broadband waveform modeling. Earth Planet. Sci. Lett. 483, 29–38.
Wells, R.E., Blakely, R.J., Sugiyama, Y., Scholl, D.W., Dinterman, P.A., 2003. Basin-centered asperities in great subduction zone earthquakes: A link between slip, subsidence, and subduction erosion? J. Geophys. Res. Solid Earth 108 (B10).
Wright, I.C., 1993. Pre-spread rifting and heterogeneous volcanism in the Southern Havre Trough back-arc basin. Mar. Geol. 113, 179–200.
Yao, H., Shearer, P.M., Gerstoft, P., 2013. Compressive sensing of frequency-dependent seismic radiation from subduction zone megathrust ruptures. Proc. Natl. Acad. Sci. 110 (12), 4512–4517.
Ye, L., Kanamori, H., Avouac, J.P., Li, L., Cheung, K.F., Lay, T., 2016. The 16 April 2016, MW 7.8 (MS 7.5) Ecuador earthquake: a quasi-repeat of the 1942 MS 7.5 earthquake and partial re-rupture of the 1906 MS 8.6 Colombia–Ecuador earthquake. Earth Planet. Sci. Lett. 454, 248–258.
Zhan, Z., Helmberger, D., Simons, M., Kanamori, H., Wu, W., Cubas, N., Culaciati, F.H.O., 2012. Anomalously steep dips of earthquakes in the 2011 Tohoku-Oki source region and possible explanations. Earth Planet. Sci. Lett. 353, 121–133.
Zhu, L., Helmberger, D.V., 1996. Advancement in source estimation techniques using broadband regional seismograms. Bull. Seismol. Soc. Am. 86 (5), 1634–1641.